Microstructure and mechanical properties of a cast TRIP-assisted multiphase stainless steel

Meng-xin Wang[1], Zi-xiang Wu[1], Jing-yu He[1], and *Xiang Chen[1, 2]

1. School of Materials Science and Engineering, Tsinghua University, Beijing 100084, China

2. Key Laboratory for Advanced Materials Processing Technology, Ministry of Education, Beijing 100084, China

Abstract: Stainless steels are used in a wide range of complex environments due to their excellent corrosion resistance. Multiphase stainless steels can offer an excellent combination of strength, toughness and corrosion resistance due to the coexistence of different microstructures. The microstructure and mechanical properties of a novel cast multiphase stainless steel, composed of martensite, ferrite, and austenite, were investigated following appropriate heat treatment processes: solution treatment at 1,050 °C for 0.5 h followed by water quenching to room temperature, and aging treatment at 500 °C for 4 h followed by water quenching to room temperature. Results show reversed austenite is formed by diffusion of Ni element during aging process, and the enrichment of Ni atoms directly determines the mechanical stability of austenite. The austenite with a lower Ni content undergoes a martensitic transformation during plastic deformation. The tensile strength of the specimen exceeds 1,100 MPa and the elongation exceeds 24% after solid solution, and further increases to 1,247 MPa and 25% after aging treatment. This enhancement is due to the TRIP effect of austenite and the precipitation of the nanoscale G-phase pinning dislocations in ferrite and martensite.

Keywords: multiphase stainless steel; mechanical properties; TRIP effect; reversed austenite; G-phase

CLC numbers: TG142.71   Document code: A   Article ID: 1672-6421(2024)03-221-08

1 Introduction

Stainless steel is commonly used in industrial facilities such as petrochemical, marine and nuclear power plants due to its excellent corrosion resistance as well as good strength and plasticity [1, 3]. As society and economy advance, the performance requirements for stainless steel have been increasing. Strength and plasticity exhibit a contradictory relationship, which necessitates a balanced approach in the design and selection of materials. Attaining high strength and high toughness has been a continuous pursuit for material researchers [4-6].

To obtain new advanced steels with higher strength and higher toughness, researchers have tried various strengthening techniques including deformation strengthening, grain refinement, and transformation strengthening, and employed the multiphase, metastable, and multiscale (M^3) microstructure control methods [7].

This understanding of M^3 can also be used to guide the development of high-performance stainless steel, especially for stainless steel castings, as their grains are relatively coarse and cannot be strengthened by means of thermal deformation.

Compared to single-phase stainless steels, duplex and multiphase stainless steels possess excellent combination of high strength and high toughness [8-11]. It has been found that the multiphase microstructure can be effectively strain partitioned to improve plasticity and toughness while ensuring high strength. In addition, the soft phase in the microstructure of the multiphase can lead to sub-crystal formation during strain partitioning, which can also improve the properties of the steel [12-14]. Microstructure containing metastable austenite can effectively hinder the crack expansion, and transform into martensite during deformation, producing TRIP effect and simultaneously improving material's strength and toughness [15-17]. Besides, introducing nanoscale precipitates into the matrix has been demonstrated an effective method for enhancing strength [18, 19]. Nanoscale precipitates can be generated by adding Cu, Al and Si on a multiphase basis by aging treatment, resulting in strengthening by nanoscale precipitations that pin dislocation during tensile deformation.

*Xiang Chen

Male, born in 1970, Ph. D., Professor. His research interests mainly focus on casting alloys, porous metals and composites. He has published over 200 papers in international and domestic journals. He is the secretary of the WFO Ferrous Metals Commission.

E-mail: xchen@tsinghua.edu.cn

In this study, a novel cast multiphase stainless steel (MPSS) containing martensite, ferrite and austenite was designed based on the Schaeffler diagram [20] and Thermo_Calc software. Schaeffler diagram was initially used to study the effect of alloying elements on the microstructure of welding metals. Because of the quick and easy prediction of microstructure, it was subsequently promoted for stainless steel composition design [21, 22]. The objective of designing such a multiphase microstructure is to enhance both the strength and plasticity of the material. To modulate the microstructure, solid solution treatment along with aging treatment was employed. The mechanical properties were assessed through tensile tests conducted at room temperature. Furthermore, transmission electron microscopy (TEM) was utilized to investigate the stabilization mechanism of austenite as well as the impact of aging precipitation strengthening. Additionally, detailed investigations were carried out on the tensile deformation characteristics and fracture behavior of this multiphase microstructure to provide valuable insights for future advancements in multiphase stainless steels development.

## 2 Experimental materials and methods

A 10 kg MPSS ingot was prepared by vacuum induction melting, and its chemical composition is listed in Table 1. The alloy compositions listed in Table 1 were substituted into the Eqs. (1) and (2) [23], and the calculated equivalent Cr_{eq} is 19.5, Ni_{eq} is 7.6. It can be seen in Fig. 1(a) that the equivalent values fall in the A+M+F three-phase region, predicting that the as-cast microstructure contains three phases: austenite, ferrite and martensite.

$$Cr_{eq}= \%Cr + \%Mo + 1.5\%Si + 0.5\%Nb \quad (1)$$

$$Ni_{eq}= \%Ni + 30\%C + 0.5\%Mn \quad (2)$$

Table 1: Chemical composition of the experiment MPSS (wt.%)

| C	Ni	Cr	Mn	Mo	Si	Cu	Nb	Fe
0.018	6.51	13.18	1.01	0.87	3.61	0.99	0.15	Bal.
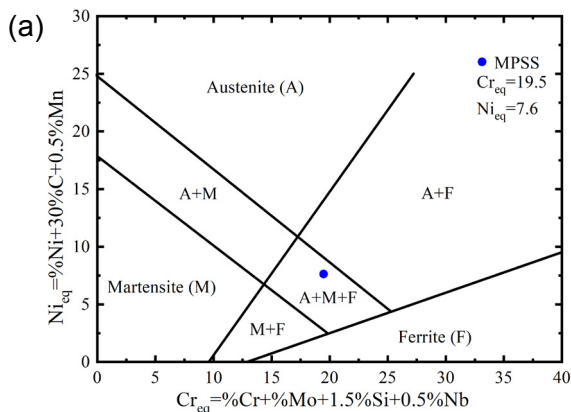
The equilibrium solidification simulation results by the Thermo_Calc software are shown in Fig. 1(b). It can be seen the δ-ferrite phase (BCC_A2) precipitates from the liquid phase at about 1,430 °C. As the temperature decreases, the liquid phase decreases and the ferrite phase increases. When the temperature decreases to 1,420 °C, the austenite phase (FCC_A1) starts to precipitate, at this time the alloy is comprised of liquid phase, δ-ferrite phase, and austenite phase. The NbC phase starts to precipitate when the temperature further decreases to around 1,080 °C. In addition, the Laves phase starts to precipitate at 810 °C, the ε-Cu phase (FCC_A1#3) starts to precipitate at 663 °C, and the G-phase starts to precipitate at 525 °C.

According to the calculated results of Thermo_Calc, the solid solution temperature was chosen at 1,050 °C to avoid the dissolution of NbC and prevent the formation of a coarse microstructure. The aging temperature was chosen to be 500 °C to form G-phase, ε-Cu and Laves phase in ferrite and martensite, which act as pinning dislocations to enhance strength.

The specimen used for microstructure observation was a 10 mm cube made by wire cutting. The solid solution treatment of the specimens was carried out by holding it at 1,050 °C for 0.5 h and water quenching to room temperature (abbreviated as S1050). After solid solution, the samples were aging treatmented 500 °C for 4 h and then water quenched to room temperature (abbreviated as AG500). The transformation of the microstructure during solidification was calculated with the help of the thermodynamic software Thermo_Calc (database: TCFE10) for a given alloy composition.

Tensile bars for testing mechanical properties have a 30 mm gauge length and a 5 mm diameter. Quasi-static testing was performed at a tensile rate of 1 mm·min⁻¹ using an electromechanical universal tensile machine (Model MTS 810). Tensile tests were repeated three times after each heat treatment and the middle value was adopted as the result. The measurement of hardness was achieved by using a Rockwell hardness tester with an applied load of 100 N. At least five indentations were made on each specimen to check for reproducibility and all mechanical experiments were conducted at the ambient temperature.
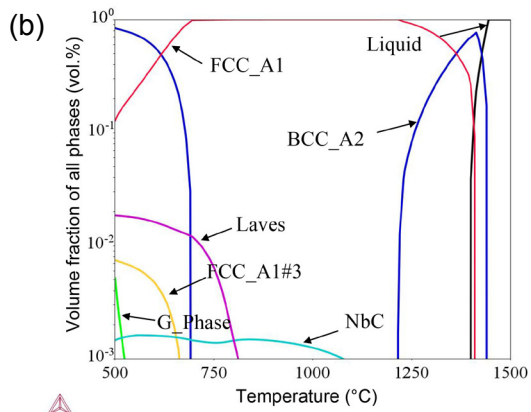
Fig. 1: Ni$_{eq}$ and Cr$_{eq}$ of MPSS in Schaeffler diagram (a) [20], and equilibrium solidification simulation of MPSS by Thermo_Calc software (b)

An X-ray diffractometer (XRD, D/max-2550), an optical microscope (OM, Zeiss-Scope. A1) and a scanning electron microscope (SEM, ZEISS-Merlin) were utilized to characterize the microstructure of MPSS. The specimen used for microstructure observation was firstly polished with 600 grit sandpaper to remove the surface wire cutting marks, and then polished with 1,000–3,000 grit abrasive papers, respectively. Then, diamond grinding paste with a particle size of 2 μm was used for polishing. Finally, the surface of specimen was etched with a mixture of 30 mL hydrochloric acid +50 g ferric chloride +70 mL deionized water for 5 s at room temperature. After etching, the specimen surface was immediately rinsed with ethanol and dried with a hair dryer. Finally, the specimen was observed with an optical microscope (OM). In RGB mode of OM, different phases will show different colors. The area percentage of ferrite was estimated by ImageJ (an open-source image processing) based on the images obtained by OM. At least five images were selected to ensure the reliability of measurements.

XRD specimens with sizes of 10 mm×10 mm×10 mm were polished using abrasive papers and mechanical polishing. The volume fraction of austenite was quantitatively measured using XRD apparatus with Cu-Kα radiation. The scanning range was from 30° to 100° with a step size of 3°·min^{-1}. The volume fraction of austenite was calculated adopting a direct comparison method by fitting the diffraction spectrums of the (200), (220) and (311) planes for the face-centered cubic (FCC) peaks, and the (220) and (211) planes for the body-centered cubic (BCC) peaks [24], based on the following Eq. (3) [25]:

$$V_\gamma = \frac{1.4I_\gamma}{1.4I_\gamma + I_a} \qquad (3)$$

where V_γ represents the volume fraction of austenite for each peak, I_γ and I_a represent the integrated intensities of the FCC and BCC peaks, respectively.

Furthermore, transmission electron microscopy (TEM, FEI Tecnai F20) equipped with energy dispersive spectroscopy (EDS) was performed to observe the characteristics of the morphology and alloy composition of reversed austenite at the acceleration voltage of 200 kV. The testing specimens were firstly reduced to a thickness of 50 μm, then made into 3 mm diameter discs, and finally prepared by ion milling with 4 kV Ar$^+$ ions at an incidence angle of 7°–8°.

3 Results

3.1 Microstructure

The metallographic microstructure and XRD results of the as-cast, solid solutioned (S1050), and aged (AG500) specimens are presented in Fig. 2. Figure 2(a) illustrates the granular and reticular morphology of the ferrite phase with a volume fraction of approximately (18.6±3.1)%. The retained austenite is mainly distributed at the edges of martensite in the as-cast specimen, accounting for a volume fraction of 26.6% [Fig. 2(d)]. Additionally, fine-grained NbC particles are primarily dispersed
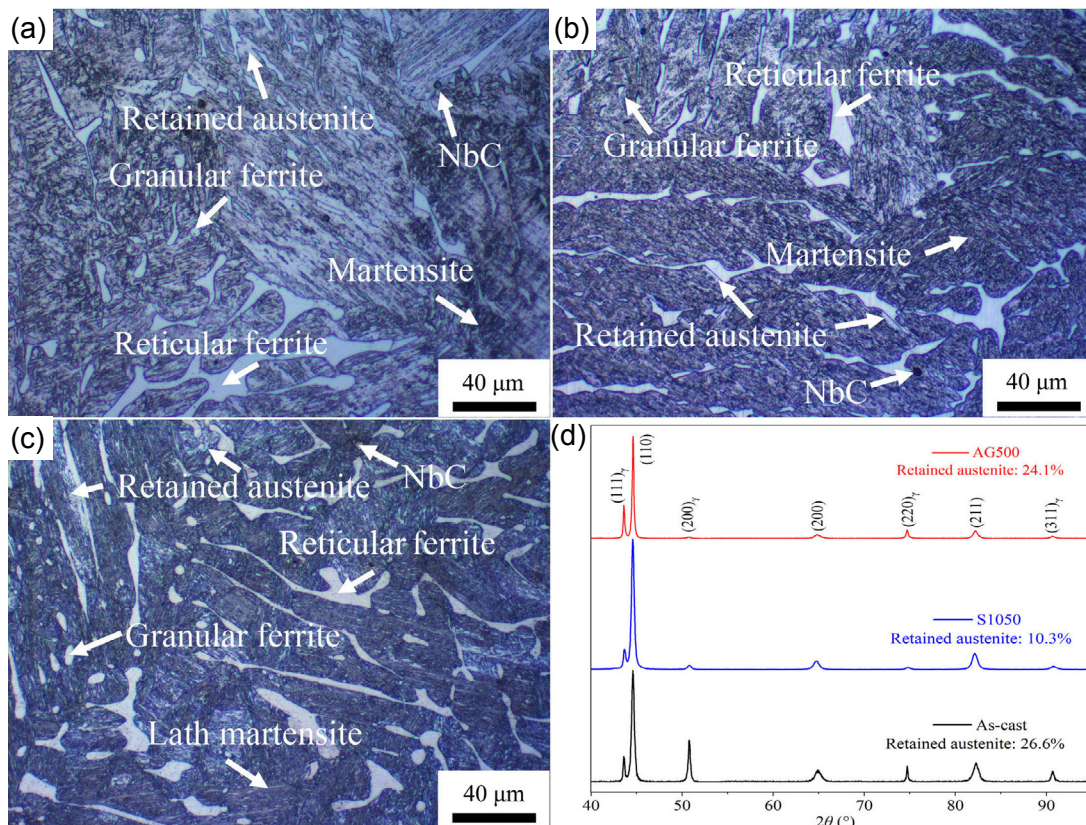

Fig. 2: Metallographic images of as-cast specimen (a), S1050 specimen (b), and AG500 specimen (c); and XRD patterns of the MPSS specimens after different heat treatments (d)

along the ferrite/martensite phase boundaries to serve as pinning constraints at negligible volume fractions, while martensite dominates the microstructure.

The microstructure after solid solution is shown in Fig. 2(b). The microstructure is dominated by quenched martensite. XRD results [Fig. 2(d)] show a reduction in austenite content after solid solution (10.3%), due to the decrease of austenite stability caused by diffusion of alloying elements. The volume fraction of ferrite is (20.5±3.6)%. Instead of dissolution, the secondary precipitates disperse along the phase boundaries. Based on Thermo_Calc calculations, the secondary precipitates can be identified as NbC.

The microstructure of the specimen after aging is shown in Fig. 2(c). It can be seen that the quenched martensite is mainly transformed into lath martensite, which is a typical characteristic of low-carbon martensitic steels. The XRD result shows an increase in austenite content to 24.1% after aging [Fig. 2(d)], indicating that some reversed austenite is formed during aging [26-28]. The ferrite remains granular and reticulated in morphology, with an increase in volume fraction to (23.1±4.1)%. The volume fraction of NbC particles and nanoscale precipitates during the aging process is negligible, thus the remained microstructure is martensite.

3.2 Mechanical properties

Figure 3 shows the engineering stress-strain curves for as-cast, solid solutioned and aged specimens. The ultimate tensile strength (UTS), yield strength (YS, 0.2% proof strength) and total elongation (TEL) of different specimens are illustrated in Table 2. The as-cast specimens have a UTS of 1,135 MPa, a lower YS of 350 MPa, and a TEL of 25.3%. The corresponding hardness value is 26.8 HRC due to the large amount of retained austenite. The curve shows a very pronounced work hardening after reaching the yield point. This is due to the TRIP effect caused by metastable austenite deformation, which can significantly increase the strength of the steel and inhibit necking, thus improving toughness [29]. After solid solution, the UTS and TEL of the specimen are almost unchanged, while the YS and HRC values are increased to 405 MPa and 30.2. This is because the TRIP effect is greatly reduced due to the reduced austenite content. After aging treatment, the UTS, YS and HRC values of the specimens are increased to 1,247 MPa, 436 MPa and 33.0, respectively, while the TEL is almost unchanged. The aging process produces reversed austenite, so there is also a significant TRIP effect during tensile process.

It is noteworthy that the yield ratios of all the three specimens are very low (Table 2). This is due to the high-volume fraction of soft phases (ferrite+austenite) in the microstructure. For the as-cast specimen, the content of ferrite and austenite is up to 45.2%. In the case of yielding, there is no precipitates which can effectively pinning dislocations in the microstructure. After solid solution treatment, the volume fraction of retained austenite decreases significantly, and the soft phase content is reduced to 35.8%. This leads to a decrease in the TRIP effect and an increase in the specimen's yield strength. After aging treatment, the volume fraction of soft phase though increases to 47.2%, the formation of nanoscale Laves phase, ε-Cu and G-phase in the microstructure can effectively pin the dislocations and improve the yield strength. Our previous study [10] reported the precipitation of Laves phase on dislocation lines in ferrite, which can effectively compensate for the lack of ferritic strength.

3.3 Fracture morphology

Figure 4 shows the tensile fracture morphologies of the as-cast, solid solutioned, and aged treatment specimens, respectively. As shown in Fig. 4(a), the macroscopic fracture of the as-cast specimen has many large secondary micro-cracks. Figure 4(b) corresponds to the microscopic fracture of the as-cast specimen characterized by a mixture of dimples and quasi-cleavages. The macroscopic fracture of the S1050 specimen shows characteristics of ductile fracture: fiber zone, radiation zone and shear lip [Fig. 4(c)]. The microscopic morphology of the S1050 specimen indicates that the fracture surface is primarily characterized by equiaxed dimples [Fig. 4(d)]. Figure 4(e) illustrates the macroscopic fracture of the AG500 specimen, exhibiting the characteristics of a typical ductile fracture with a greater degree of deformation and no secondary micro-cracks. The microscopic morphology of the AG500 specimen also indicates that the fracture surface mainly consists of equiaxed dimples [Fig. 4(f)].
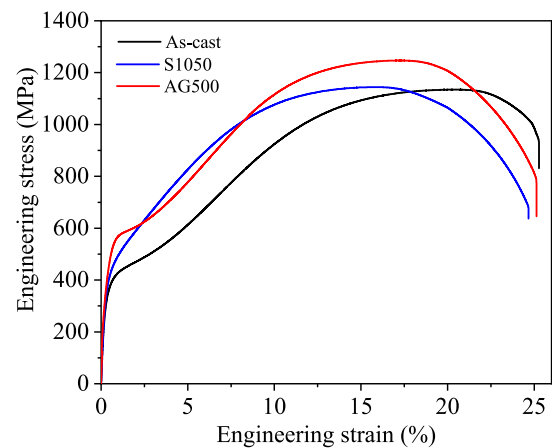

Fig. 3: Engineering stress-strain curves of the specimens

Table 2: Mechanical properties of MPSS at different states

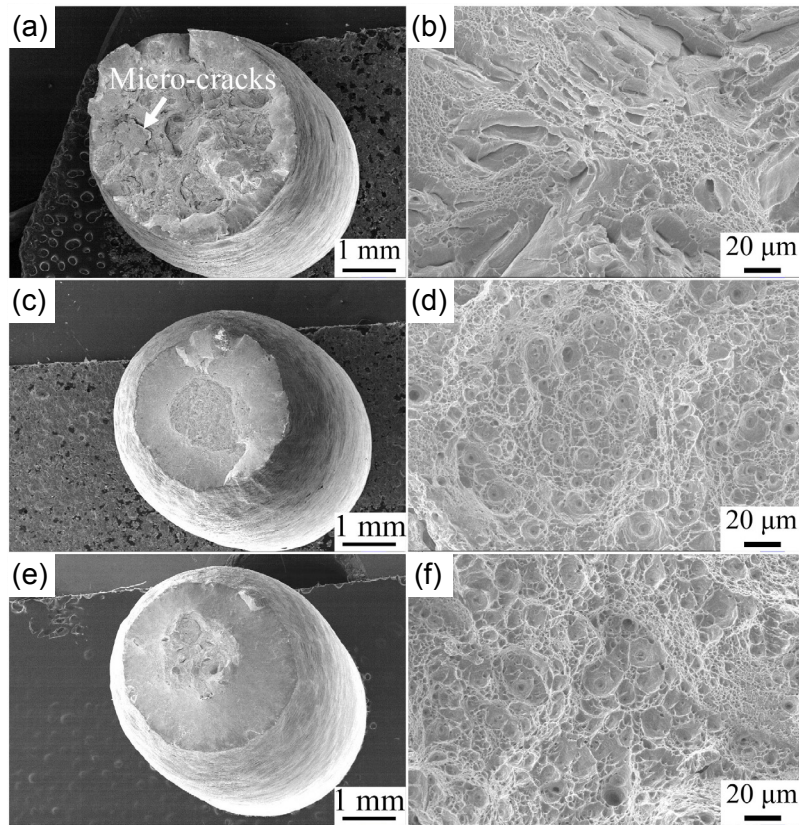| Specimen	UTS (MPa)	YS (MPa)	Yield ratio	TEL (%)	HRC
As-cast	1,135	350	0.31	25.3	26.8±2.2
S1050	1,144	405	0.35	24.7	30.2±1.8
AG500	1,247	436	0.35	25.1	33.0±1.2

Fig. 4: SEM micrographs of macroscopic fracture surface of as-cast (a), S1050 (c), and AG500 (d) specimens; and microscopic fracture surface of as-cast (b), S1050 (d), and AG500 (f) specimens

4 Discussion

4.1 Reversed austenite formation and stabilization

Reversed austenite has been shown to inhibit cracking and improve the toughness of steels, and MPSS specimens can be aged to obtain more than 10% reversed austenite with significant TRIP effect in tensile process, allowing the aged specimen to retain the high strength and an elongation of over 25%. Figure 5(a) shows the TEM micrograph of the aged specimen, which has not undergone any tensile deformation. The martensite is lath-like and has a high density of dislocations. Between the laths there is a thin film of austenite with a thickness of 100–200 nm. The thin film of austenite has higher Ni and Cu contents by EDS and is identified as reversed austenite. Figure 5(b) shows the TEM micrograph of the aged specimen after tensile deformation. The martensite is also distributed in laths, and the density of dislocations within the laths is increased due to deformation. It is also shown in Fig. 5(b) that the thin film-like austenite does not fully transform into martensite under stress after deformation. The positions in the white dashed areas show the occurrence of transformation, while the adjacent part remains untransformed. This indicates that the mechanical stability of the reversed austenite is not uniform. The EDS results show that the Ni content at Position P1 is lower compared to that at Position P2 [as shown in Figs. 5(c) and (d)]. Nickel is an important element for the formation and stabilization of austenite. This study reveals that in the thin film austenite, Ni is not evenly distributed, leading to less stability and a greater tendency for martensitic transformation in austenites with a lower Ni content during plastic deformation.

4.2 Multiphase deformation and failure

Figure 6 shows the true stress-strain curves and the corresponding work hardening curves for the as-cast, solid solutioned, and aged MPSS specimens. Based on the work hardening curves in Fig. 6, it can be seen that the work hardening rates of all the three specimens experience three stages: rapidly decrease (Stage A), then increase (Stage B), and finally significantly decrease (Stage C). However, there are significant differences between these specimens. For S1050 specimen, the value of work hardening rate at Stage A ($\varepsilon_T<2.11\%$) decreases slowly, followed by a relatively insignificant increase at Stage B (2.11%–3.44%) with increasing strain, and then the work hardening rate decreases greatly, where the onset of necking leading to the fracture. Compared with the S1050 specimen, the work hardening rate of as-cast and the AG500 specimens at Stage A ($\varepsilon_T<1.99\%$) decreases more rapidly, and the corresponding minimum work hardening rates are much lower than that of the S1050 specimen. The work hardening rate of the as-cast and the AG500 specimens increases gradually at Stage B. The work hardening rate of the AG500 specimen increases more rapidly, indicating that the TRIP effect of the AG500 specimen is more pronounced than that of the as-cast specimen. In the final Stage C, the AG500 specimen shows a more rapid decreases in work hardening rate due to reduced
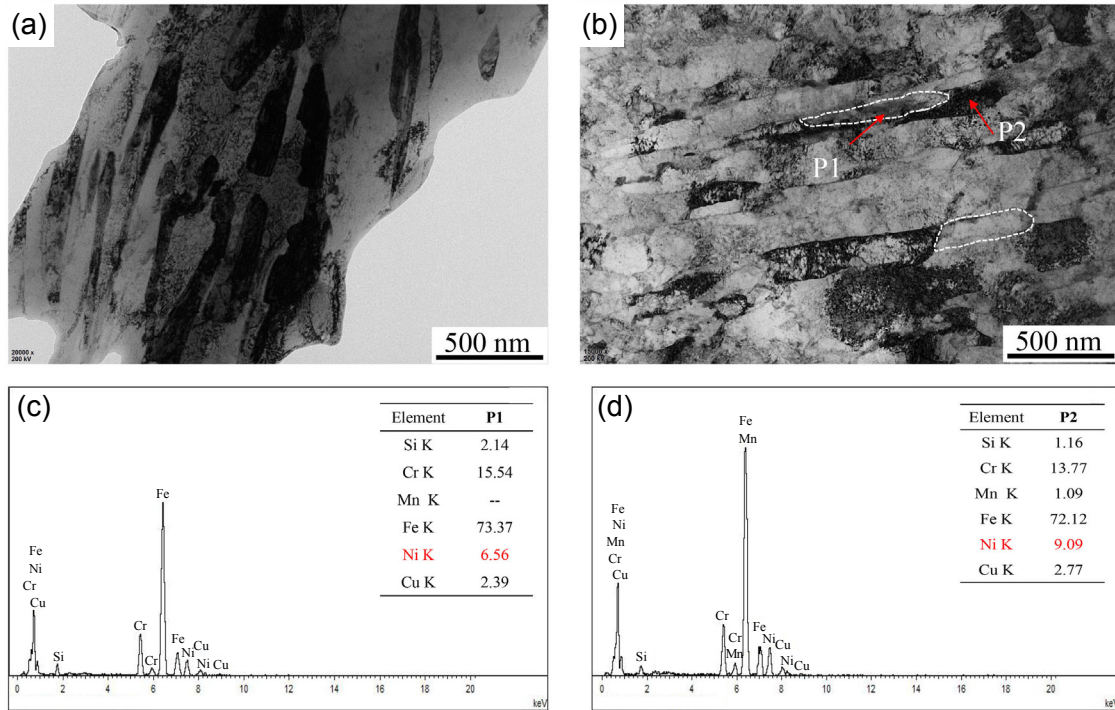
Fig. 5: TEM micrographs of reversed austenite before (a) and after (b) tensile deformation, and EDS results corresponding to P1 (c) and P2 (d) in Fig. 5(b)

plasticity caused by precipitation strengthening. Arrows in Fig. 6 indicate the instability for necking of different samples. When the true strain reaches 18.8%, the as-cast specimen undergoes necking. When the true strain is 16.3%, the AG500 specimen begins to go through necking. For the S1050 specimen, necking starts at a true strain of 14.6%. This is mostly because of less austenite content in the S1050 specimen, lowering the TRIP effect, resulting in reduced inhibition of necking.

Figure 7 shows the SEM micrographs near the fracture of the as-cast, S1050 and AG500 specimens. For the as-cast specimen, the cracks occur mainly in the phase boundaries and inside the ferrite, as shown in Figs. 7(a, b). The cracks at the phase boundaries are mainly caused by precipitated NbC [8], while the cracks within the ferrite are caused by the granular precipitates. EDS result and previous literature indicate that this precipitate is a Laves phase with high Si and Mo contents [10], as shown in Fig. 7(b). Laves phase is a hard and brittle phase at room temperature, which can damage the toughness of the material [30].
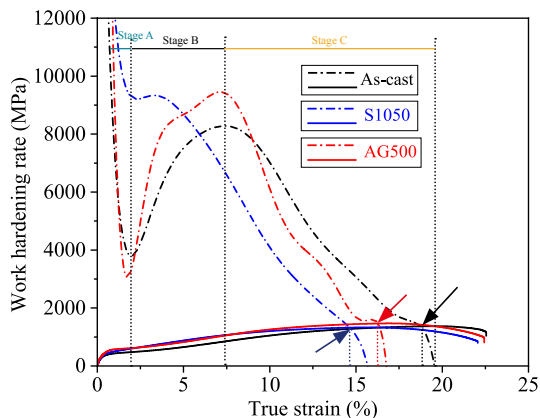
After solid solution treatment, dissolution of Laves phase occurs, so that crack at the phase boundaries and inside the ferrite is greatly reduced, as shown in Fig. 7(c). Figure 7(d) shows the microstructure near the fracture of the AG500 specimen. Severe deformation occurs within the lath martensite and ferrite. The formation of cracks at phase boundaries is mainly due to discrepancies in the deformation of soft phase ferrite and hard phase martensite, leading to stress concentration and subsequent cracking at these boundaries [14, 31]. Additionally, the brittle nature of NbC particles at phase boundaries makes them especially susceptible to cracking and further propagation of the crack [8].

Figures 8(a) and (b) show the TEM micrographs of the martensite and ferrite phases in the AG500 specimen. Nanoscale G-phase particles are diffusely distributed in the martensite and ferrite, which can constrain dislocation motion during deformation. G-phase is an intermetallic silicide that has been observed in many precipitation hardened stainless steels and duplex stainless steels [32, 33]. The high-resolution transmission electron microscopy (HRTEM) micrograph indicates that the G-phase has a square-like shape (15 nm ×16 nm), and the lattice parameters are 1.12 nm and 1.14 nm [34], as shown in Fig. 8(c). Figure 8(d) is the SAED result corresponding to Fig. 8(c). It indicates that the G-phase is coherent with the matrix. This nanoscale precipitation has been shown to provide significant strength to the steel with less damage to the toughness [19, 35].

5 Conclusions

A new cast multi-phase stainless steel containing martensite, ferrite, and austenite was prepared through solution and aging heat treatment. The investigated stainless steel exhibits superior properties due to the mixed microstructure of hard
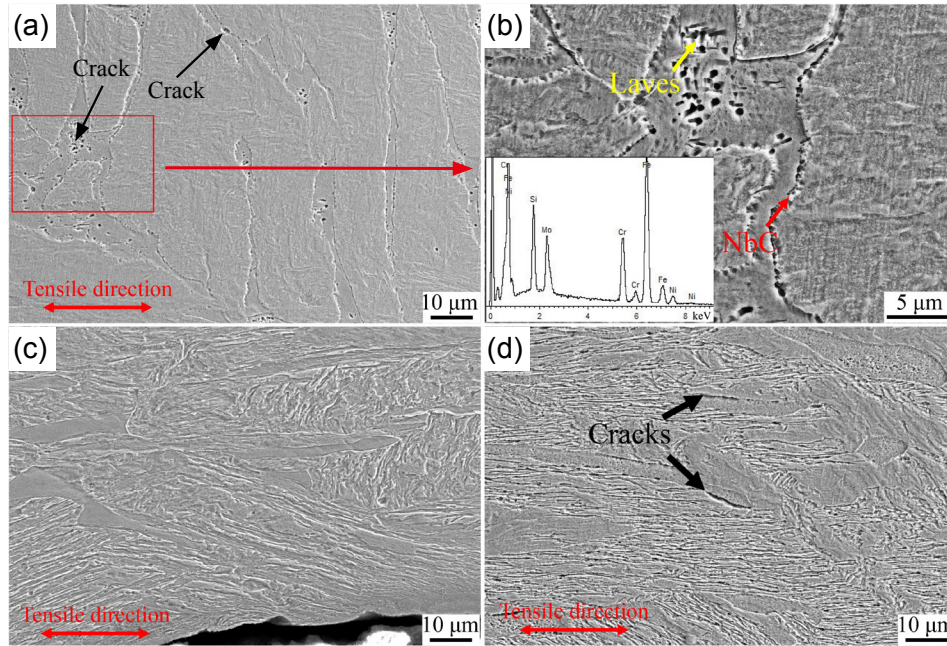

Fig. 6: Work hardening rate as a function of true strain

Fig. 7: SEM micrographs of lateral fracture of the as-cast (a), S1050 (c) and AG500 (d) specimens, and (b) is the enlarge view of (a)
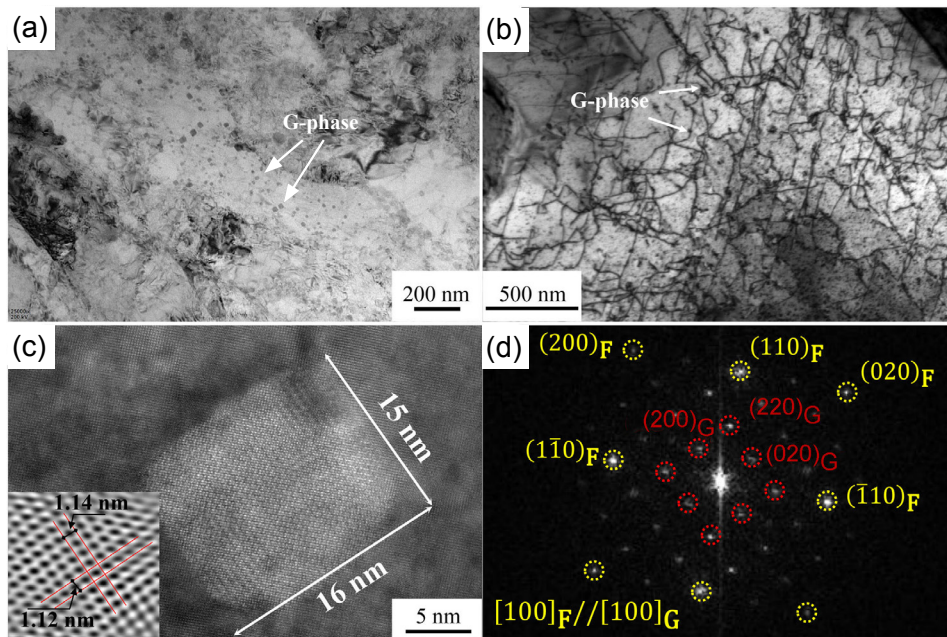

Fig. 8: TEM micrograph of G-phase precipitating in martensite (a) and ferrite (b), and HRTEM micrograph of G-phase (c). The inserted graph in (c) indicates the SAED result (d) of G-phase

and soft phases, the TRIP effect of metastable austenite, and the nanoscale precipitation of aging treatment. Based on the experimental results, the following conclusions can be drawn:

(1) By restricting the alloy composition to the martensite + ferrite + austenite three-phase region in the Schaeffler diagram, a mixed microstructure consisting of both hard and soft phases can be achieved in the as-cast condition, which ensures a combination of high toughness and strength.

(2) Reversed austenite is formed by the diffusion of Ni between martensitic laths during aging. It exists as a thin film (100–200 nm) with a non-uniform distribution of Ni. The austenite with a lower Ni content undergoes a martensitic

transformation during plastic deformation.

(3) The aged specimen has the best combination of strength and elongation (UTS: 1,247 MPa, TEL: 25.1%). This enhancement is attributed to the TRIP effect of austenite and the precipitation of the nanoscale G-phase which can pin the dislocations in ferrite and martensite.

Acknowledgment

Conflict of interest

The authors declare that they have no known competing financial interests or personal relationships that could have appeared to influence the work reported in this paper.

References

[1] Zhu Z H, Zhang W D, Tu X H, et al. Effect of sigma phase precipitation on microstructure and properties of cast ZG0Cr26Ni5Mo3Cu3 duplex stainless steel under different heat treatments. China Foundry, 2018,15(3): 182–188.

[2] Lo K H, Shek C H, Lai J K L. Recent developments in stainless steels. Materials Science and Engineering: A, 2009, 65: 39–104.

[3] Di Schino A. Manufacturing and applications of stainless steels. Metals, 2020, 10: 327–329.

[4] Li Y, Zhao Y Q, Zeng W D, et al. Effect of heat treatment process on the microstructure and properties of 2Cr13 stainless steel. Foundry, 2022, 71(11): 1364–1367. (In Chinese)

[5] Sohrabi M J, Naghizadeh M, Mirzadeh H. Deformation-induced martensite in austenitic stainless steels: A review. Archives of Civil and Mechanical Engineering, 2020, 20: 124–143.

[6] Lan K, Ding W, and Yang Y T. Effect of heat treatment on microstructure and mechanical properties of Ti-containing low alloy martensitic wear-resistant steel. China Foundry, 2022, 20(4): 329–338.

[7] Xie Z J, Shang C J, Wang X I, et al. Recent progress in third-generation low alloy steels developed under M^3 microstructure control. International Journal of Minerals, Metallurgy and Materials, 2020, 27: 1–9.

[8] Wu Z, Wang M, He J, et al. A novel cast multiphase stainless steel with high strength and high toughness. Metallurgical and Materials Transactions: A, 2023, 54: 2617–2630.

[9] He Q, Wang Y F, Wang M S, et al. Improving strength-ductility synergy in 301 stainless steel by combining gradient structure and TRIP effect. Materials Science and Engineering: A, 2020, 780: 139146.

[10] Wu Z, Liu Y, Zhang H, et al. Microstructure and mechanical properties of a novel cast multi-phase stainless steel. Journal of Materials Research and Technology, 2022, 19: 4177–4182.

[11] Song Y, Li C, Liao Y, et al. Effects of tempering temperature on the microstructure evolution and mechanical properties of 16%Cr-5%Ni super martensitic stainless steel. Journal of Materials Research and Technology, 2023, 24: 9306–9322.

[12] Kratochvíl J, Sedláček R. Energetic approach to subgrain formation. Materials Science and Engineering: A, 2004, 387–389: 67–71.

[13] Wang N, Chen Y, Wu G, et al. Investigation on micromechanism involved in ferrite hardening after prestraining of dual-phase steel. Materials Science and Engineering: A, 2021, 800: 140387.

[14] Wu Z, Wang M, He J, et al. Strain partitioning in ferrite and mechanical properties of a cast multiphase stainless steel. Materials Today Communications, 2023, 35: 105644.

[15] Govindaraj V, Hodgson P, Singh R P, et al. The effect of austenite reversion on the microstructure and mechanical properties of a 12Cr-3Ni-3Mn-3Cu-0.15Nb-0.05C maraging stainless steel. Materials Science and Engineering: A, 2021, 828: 142097.

[16] Wang P, Xiao N, Lu S, et al. Investigation of the mechanical stability of reversed austenite in 13%Cr-4%Ni martensitic stainless steel during the uniaxial tensile test. Materials Science and Engineering: A, 2013, 586: 292–300.

[17] Niu M C, Yang K, Luan J H, et al. Cu-assisted austenite reversion and enhanced TRIP effect in maraging stainless steels. Journal of Materials Science & Technology, 2022, 104: 52–58.

[18] Xu S S, Lu X H, Liu S C, et al. Precipitation strengthening of Cu/NiAl co-precipitates in a martensite-austenite dual-phase steel. Materials Characterization, 2021, 182: 111589.

[19] Yang M, Wang C, Yang S, et al. New insights into the precipitation strengthening of ferritic steels: Nanoscale G-phase particle. Materials Letters, 2017, 209: 134–137.

[20] Chen X, Li Y. Fracture toughness improvement of austempered high silicon steel by titanium, vanadium and rare earth elements modification. Materials Science and Engineering: A, 2007, 444: 298–305.

[21] Wang P, Zheng W, Dai X, et al. Prominent role of reversed austenite on corrosion property of super 13Cr martensitic stainless steel. Journal of Materials Research and Technology, 2023, 22: 1753–1767.

[22] Schaeffler A L. Constitution diagram for stainless steel weld metal. Metal progress, 1949, 56(11): 680.

[23] Chen S R, Davies H A, Rainforth W M. Austenite phase formation in rapidly solidified Fe-Cr-Mn-C steels. Acta Materialia, 1999, 47: 4555–4569.

[24] Johnson E, Gråbæk L, Johansen A, et al. Microstructure of rapidly solidified stainless steel. Materials Science and Engineering, 1988, 98: 301–303.

[25] Suutala N, Takalo T, Moisio T. Ferritic-austenitic solidification mode in austenitic stainless steel welds. Metallurgical Transactions A, 1980, 11(5): 717–725.

[26] Zhang H, Mi P, Hao L, et al. Evolution of toughening mechanisms in PH13-8Mo stainless steel during aging treatment. Materials (Basel), 2023, 16: 3630–3644.

[27] Chen C Y, Chiu P H, Liu W S, et al. Interaction between η-Ni_3Ti and reversed austenite within Custom 465 stainless steel: Experimental evidence and related patents investigation. Materials Science and Engineering: A, 2022, 839: 142852.

[28] Zhang H, Ji X, Ma D, et al. Effect of aging temperature on the austenite reversion and mechanical properties of a Fe-10Cr-10Ni cryogenic maraging steel. Journal of Materials Research and Technology, 2021, 11: 98–111.

[29] Chiang J, Lawrence B, Boyd J D, et al. Effect of microstructure on retained austenite stability and work hardening of TRIP steels. Materials Science and Engineering: A, 2011, 528: 4516–4521.

[30] Sello M P, Stumpf W E. Laves phase embrittlement of the ferritic stainless steel type AISI 441. Materials Science and Engineering: A, 2010, 527: 5194–5202.

[31] Song C, Yu H, Lu J, et al. Stress partitioning among ferrite, martensite and retained austenite of a TRIP-assisted multiphase steel: An in-situ high-energy X-ray diffraction study. Materials Science and Engineering: A, 2018, 726: 1–9.

[32] Guo X F, Ni Y Y, Gong J M, et al. Formation of G-phase in 20Cr32Ni1Nb stainless steel and its effect on mechanical properties. Acta Metallurgica Sinica (English Letters), 2017, 30: 829–839.

[33] Chen Y, Dai X, Chen X, et al. The characterization of G-phase in Fe20Cr9Ni cast duplex stainless steel. Materials Characterization, 2019, 149: 74–81.

[34] Shuro I, Kuo H H, Sasaki T, et al. G-phase precipitation in austenitic stainless steel deformed by high pressure torsion. Materials Science and Engineering: A, 2012, 552: 194–198.

[35] Yang M, King D J M, Povstugar I, et al. Precipitation behavior in G-phase strengthened ferritic stainless steels. Acta Materialia, 2021, 205: 116542.